



Efficient Pt/carbon electrocatalysts for proton exchange membrane fuel cells: Avoid chloride-based Pt salts!



Nathalie Job^{a,*}, Marian Chatenet^b, Sandrine Berthon-Fabry^c, Sophie Hermans^d, Frédéric Maillard^b

^a Université de Liège, Laboratoire de Génie chimique-Génie catalytique (B6a), B-4000 Liège, Belgium

^b Laboratoire d'Electrochimie et de Physico-chimie des Matériaux et des Interfaces (LEPMI), UMR 5279 CNRS/Grenoble-INP/Université de Savoie/Université Joseph Fourier, BP75, F-38402 St Martin d'Hères Cedex, France

^c MINES ParisTech, PERSEE- Centre procédés, énergies renouvelables et systèmes énergétiques, CS 10207 rue Claude Daunesse, 06904 Sophia-Antipolis Cedex, France

^d Institut de la Matière Condensée et des Nanosciences, Université catholique de Louvain, Place Louis Pasteur 1/3, B-1348 Louvain-la-Neuve, Belgium

HIGHLIGHTS

- Pt/C catalysts were prepared by impregnation of carbon xerogels with H₂PtCl₆.
- Due to incomplete decomposition, Cl ions poison Pt.
- The effect of Cl ions on CO_{ads} oxidation and O₂ reduction was investigated.
- The Cl ions impact negatively the reaction rate.
- For efficient PEM fuel cell catalysts, Cl-containing precursors must be avoided.

ARTICLE INFO

Article history:

Received 29 October 2012

Received in revised form

13 February 2013

Accepted 27 March 2013

Available online 10 April 2013

Keywords:

PEM fuel cells

Oxygen reduction reaction

Pt catalysts

Carbon xerogel

Chloride

Contamination

ABSTRACT

The catalytic layers of Proton Exchange Membrane (PEM) fuel cells use carbon-supported Pt-based nanoparticles, which are classically synthesized by impregnation with a metal precursor usually based on chloride counter-ions. However, the literature points out that chloride ions poison the catalytic activity. The purpose of this work is to compare the surface reactivity and the electrocatalytic activity of Pt/carbon xerogel nanoparticles contaminated with different amount of chlorine. The catalysts were synthesized using the Strong Electrostatic Adsorption (SEA) method and H₂PtCl₆ as a metal precursor. The Cl content in the catalysts was changed by varying the gas atmosphere and the duration of the reduction step. The effect of Cl contamination was investigated on two model reactions: the electrochemical CO_{ads} oxidation and the O₂ reduction. Evidences are provided that the Cl⁻ ions issued from the incomplete decomposition/removal of the metal precursor partially block the Pt catalytic sites, and limit the rate of the CO_{ads} + OH_{ads} recombination and of the diffusion of CO_{ads} molecules in CO stripping experiments. The adsorption of Cl⁻ ions also depreciates the ORR kinetics. In search for efficient catalysts, chloride-containing metal precursors must therefore be avoided.

© 2013 Elsevier B.V. All rights reserved.

1. Introduction

Carbon-supported platinum nanoparticles (Pt/C) remain the material of choice for the preparation of catalytic layers in Proton Exchange Membrane (PEM) fuel cells. A large variety of elaboration techniques are available in the literature: wet and dry impregnation [1,2], ion exchange [3,4], vapour phase deposition [5], or plasma processes [6–8]. However, technical constraints specific to

electrocatalysis in PEM fuel cells strongly narrow the choice of the Pt/C preparation technique. Indeed, the catalytic layers, usually composed of Pt/carbon black, gas voids and ionomer, (hot-)pressed between a proton-exchange membrane and a diffusion layer (carbon felt) [9], must be relatively thin to minimize both the ohmic losses caused by proton transport and the losses due to mass transport of reactants and products [10]. These phenomena, as well as the sluggish rate of the ORR, are generally overcome by the use of catalysts with a high Pt weight fraction, ranging from 20 to 80 wt.%.

The techniques based on the deposition of metal from the gas phase, well adapted to flat surfaces or non-porous carbon supports,

* Corresponding author. Tel.: +32 4366 3537; fax: +32 4366 3545.

E-mail address: Nathalie.Job@ulg.ac.be (N. Job).

such as carbon fibres or nanotubes, are not appropriate for porous substrates, because metal precursors hardly penetrate the pores of the carbon particles; for instance, the depth of penetration remains below 1 μm for plasma sputtering [6,7]. Therefore, the preparation of highly loaded Pt/C electrocatalysts (on porous carbon supports, such as carbon blacks), is preferably undergone using impregnation in liquid phase and further reduction.

Another important aspect to design efficient PEM fuel cells catalytic layers is to consider their architecture, and especially the pore texture of the carbon support. The pore structure of the catalytic layers not only depends on the nature of the carbon support, but also on the electrode processing [11–15]. Thus, in carbon-black-based air-fed cathode, where oxygen, proton and water transports are involved in the ORR, high potential losses due to diffusional limitations offset the cell performance [10,16]. This is why researches target the elaboration of porous carbon materials with appropriate, processing-independent pore texture that could replace carbon blacks as electrocatalyst supports.

Among the numerous new carbon materials that can be found in the literature, carbon aerogels and xerogels are ideally suited to replace carbon blacks [13,17–19]. Indeed, their pore texture can be adjusted within a wide range (from a few nm up to a few μm with large pore volume [20,21]) and it has been demonstrated that internal diffusional limitations in gas phase heterogeneous catalysis can be suppressed by replacing activated carbon supports by carbon gels [22]. Several studies have shown that the diffusion overpotential of PEM fuel cells prepared with carbon gel-supported Pt catalysts is strongly dependent on the pore texture of the carbon support [13,17,18]: using materials with appropriate pore size and pore volume lead to the decrease of the diffusional limitations, and possibly to a better contact between the Pt particles and the ionomer [23].

The Pt/carbon gel catalysts are classically obtained via deposition from the liquid phase; in most cases, impregnation of the support by H₂PtCl₆ solutions is used and followed by various post-treatments such as liquid phase reduction [13,17] or drying followed by gas phase reduction under hydrogen [18,23]. The 'Strong Electrostatic Adsorption' (SEA) method was previously developed to prepare Pt/carbon xerogel catalysts exhibiting high Pt dispersion at high metal content [23,24]. The SEA method [25] consists in maximizing the electrostatic interactions between the metal precursor and the support by adjusting the pH of the carbon/water/Pt precursor slurry to the adequate value, which depends on both the surface chemistry of the support and the nature of the Pt precursor. In the case of impregnation of carbon xerogels with H₂PtCl₆ aqueous solutions (1000 ppm_{Pt}), the initial pH leading to the highest Pt uptake was found to be 2.5, and the corresponding maximum Pt weight percentage ranged from 8 to 10 wt.%, with very homogeneously dispersed nanoparticles around 2–3 nm in size after reduction with H₂ at 200 °C [23,24]. The metal weight percentage can be increased up to 20–30 wt.% by repeated impregnation–drying–reduction sequences. During the second or third sequence, new Pt nanoparticles are deposited on the support without affecting the metal dispersion and all the observed particles remain very well dispersed (2–3 nm) while the particle surface concentration increases [23].

However, it was noticed that, when using H₂PtCl₆, which is the most common precursor in impregnation techniques, the catalytic activity of the dispersed Pt/carbon xerogel catalysts was dramatically low compared to inhomogeneous Pt/carbon gel catalysts presenting much lower metal dispersion [23]. Furthermore, it was also shown that, by increasing the final reduction temperature of the catalysts from 200 °C to 450 °C, the fuel cell performance

increased largely, which hinted at contamination of the Pt catalytic sites by chlorine atoms and cleaning of the metal surface by high temperature reduction. The oxidation state and the location of the chlorine atoms remained to a large extent unclear but the above effects strongly pointed towards Cl[−] (chloride) ions adsorbed on or at close proximity of the Pt nanoparticles.

The aim of the present paper is to gain more insights on how chloride ions influence the surface reactivity and the electrocatalytic activity of carbon-supported Pt nanoparticles for two model reactions of interest for PEM fuel cell electrocatalysis: the electrochemical CO_{ads} oxidation and the oxygen reduction reaction (ORR). For that purpose, Pt/carbon xerogel catalysts were prepared by the SEA method using H₂PtCl₆ as a precursor, and further post-treated under various temperature and atmosphere conditions. The samples were characterized by physico-chemical and electrochemical methods, and used as catalysts in model and real PEM fuel cell cathodes.

2. Experimental

2.1. Support and catalyst preparation

All the procedures, from material synthesis to complete pore texture characterization, are detailed in Ref. [23]. The carbon support chosen for this study was a micro-macroporous carbon xerogel with a macropore size ranging from 50 to 85 nm, a total pore volume equal to 2.1 cm³ g^{−1} and a micropore volume of 0.26 cm³ g^{−1}. The specific surface area of the support was 643 m² g^{−1}. The carbon support was prepared by drying and pyrolysis of a resorcinol-formaldehyde gel. This type of synthesis yields very clean carbon materials containing very low ash content (<0.5 wt.%, sodium carbonate mostly) and very low oxygen surface groups [26].

Briefly, the aqueous gel was first obtained by polycondensation of resorcinol (Vel, 99%) with formaldehyde (Aldrich 37 wt.% in water, stabilized with 10–15 wt.% methanol) in water, in the presence of Na₂CO₃ (UCB, 99.5%). The resorcinol/formaldehyde molar ratio, R/F, was fixed at 0.5, which is usually considered as the stoichiometric ratio [27]. The resorcinol/sodium carbonate molar ratio, R/C, was equal to 1000, while the solvents/(resorcinol + formaldehyde) molar ratio, D, was chosen equal to 5.7. In D, the term 'solvents' includes the deionized water added, and the water and methanol (stabilizer) present in the formaldehyde solution. Gelation and ageing were performed at 85 °C for 72 h. The wet material was dried by evaporation at 60 °C in a vacuum oven, the pressure being reduced from 10⁵ Pa to 10³ Pa over 2 days. The sample was then left at 150 °C and 10³ Pa for 12 h. Finally, the carbon xerogel was obtained by pyrolysis at 800 °C for 2 h under nitrogen flow [23].

The pristine Pt/C catalyst was prepared by impregnation with H₂PtCl₆, using the SEA method [25]. The optimal impregnation conditions for carbon xerogels were determined in a previous study [24]. The carbon support was first impregnated with an H₂PtCl₆ aqueous solution (4.1 mmol L^{−1}), the pH of which was adjusted to 2.5 with HNO₃ prior to carbon addition. The total material surface area in solution, i.e. the surface loading (SL), was fixed at 10³ m² L^{−1}. So, 3.7 g of carbon xerogel (643 m² g^{−1}) was mixed with 2.38 L of H₂PtCl₆ solution. After 1 h under magnetic stirring, the slurry was filtered and the recovered solid was dried in air at 100 °C for 12 h. The catalyst obtained was then reduced under flowing H₂ (0.04 mmol s^{−1}) at 200 °C for 1 h. In order to increase the Pt weight percentage up to 15 wt.%, this impregnation–drying–reduction cycle was done twice on the same catalyst batch. Indeed, it was shown that repeating the cycle up to three times does not modify the Pt dispersion [23]: the obtained

catalyst is composed of very homogeneously dispersed Pt particles about 2 nm in size, whatever the metal loading (at least up to 23.5 wt.%).

The obtained catalyst is labelled H2-200-1, according to the reductive atmosphere, temperature and duration, and was further post-treated.

2.2. Catalyst post-treatments

The pristine catalyst reduced at 200 °C (H2-200-1) is strongly poisoned with chlorine [23]. In order to decrease the amount of Cl present at the Pt surface, sample H2-200-1 was post-treated at various temperatures, either under hydrogen (for temperatures lower than 500 °C) or helium (above 500 °C) flow (0.04 mmol s⁻¹). Two samples were prepared by reduction for 3 h at 350 and 450 °C (samples H2-350-3 and H2-450-3). However, it was previously demonstrated that chlorine is still present even after treatment under hydrogen at 450 °C for 5 h (see sample X-Pt-2/450 in Ref. [23]). In addition, above 500 °C (H₂ atmosphere), the carbon support begins to degrade by gasification and the Pt nanoparticles sinter [28]; as a result, both the pore texture and metal dispersion are modified. This phenomenon hampers the use of temperatures above 500°C in reducing atmosphere. In order to completely remove chlorine, two samples were prepared from the raw catalyst, sample H2-200-1, by thermal treatment under flowing helium at 650 °C and 750 °C during 3 h (He-650-3 and He-750-3). The post-treatment conditions of all samples are gathered in Table 1. For reference, a sixth sample (X-Pt-2/450 from Ref. [23]) was added; this sample, issued from another batch, was prepared in the exact same way on the same support and reduced for 5 h at 450 °C under hydrogen flow.

2.3. Physico-chemical characterization of the support and catalysts

The metal content of the pristine catalyst, H2-200-1, was measured by Inductively Coupled Plasma-Atomic Emission Spectrometry (ICP-AES, Iris advantage Thermo Jarrel Ash). Experimental details about Pt digestion and analysis can be found in Ref. [29]. In order to measure the particle size distribution, the catalysts were investigated by transmission electron microscopy, with a JEOL 2010 apparatus operated at 200 kV with a point-to-point resolution of 0.19 nm (LaB₆ filament). The samples were crushed and dispersed in ethanol and subsequently deposited onto a Lacey-carbon/Formvar copper grid (PELCO). Particle size distributions as well as the associated standard deviation, σ , were obtained by image analysis [23] performed on a set of at least 1000 particles. The surface weighted average diameter, $d_s = \sum n_i d_i^3 / \sum n_i d_i^2$, and the volume weighted average diameter, $d_v = \sum n_i d_i^4 / \sum n_i d_i^3$, where n_i is

the number of particles of diameter d_i , were calculated for comparison with the other characterization methods [30]. The metal particles were also analysed by X-ray diffraction (XRD) with a Siemens D5000 goniometer using the Cu-K α line (Ni filter). The average metal particle size, d_{XRD} , was estimated using Scherrer's equation [30].

A volumetric static method was used for CO chemisorption [30,31]. Measurements were obtained on a Fisons Sorptomatic 1990 equipped with a turbomolecular vacuum pump that allows reaching a high vacuum of 10⁻³ Pa. After post-treatment (see Section 2.2), the samples were outgassed for 16 h at room temperature and 10⁻³ Pa. Carbon monoxide adsorption was then performed at 30 °C. Since both chemisorption (on the Pt surface atoms) and physisorption (on metallic sites and support surface) occur at the catalyst surface, it is necessary to separate chemisorption and physisorption effects. A first CO adsorption isotherm was achieved so as to measure the total amount of adsorbed carbon monoxide (chemisorbed + physisorbed). The catalyst was then outgassed on the measurement unit at 30 °C for 2 h in a vacuum of 10⁻³ Pa, and a second CO adsorption isotherm was measured in order to evaluate the amount of physisorbed CO. The total CO chemisorbed amount was deduced by subtracting the second isotherm from the first one and extrapolating the nearly horizontal difference curve to the uptake axis.

The samples were analysed by X-ray photoelectron spectroscopy (XPS), performed on an SSI-X-probe (SSX-100/206) spectrometer from Fisons. The samples were stuck onto troughs with double-sided adhesive tape and placed on an insulating homemade ceramic carousel with a nickel grid 3 mm above the samples, to avoid differential charging effects. A flood gun set at 8 eV was used for charge stabilisation. The energy scale was calibrated by taking the Au 4f_{7/2} binding energy at 84 eV. The C1s binding energy of carbon contamination set at 284.8 eV was used as internal standard value. Data treatment was performed with the CasaXPS program (Casa Software Ltd).

2.4. Electrochemical characterization of the catalysts

The electrochemically active Pt surface area of the samples and their electrocatalytic activity for the ORR were determined in aqueous electrolyte using a rotating disk electrode (EDT 101, Tacussel). The experiments were carried out on a thin active layer (AL) of Pt/C catalyst deposited onto a glassy carbon electrode. In each case, the AL was prepared from a suspension blended from 23.3 mg of catalyst, 466 mg of 5 wt.% Nafion® in alcohol (Aldrich), and 0.755 mL of ultrapure water (18.2 MΩ cm – 3 ppb total organic compounds, Millipore Elix + Gradient). After homogenization in an ultrasonic bath for 1 h, 10 μL of the suspension was deposited on the

Table 1
Physico-chemical characterization of the catalysts.

Sample	XRD		TEM			XPS Cl/Pt	CO chemisorption			
	d_{XRD} (nm)	d_{TEM} (nm)	σ (nm)	d_s (nm)	d_v (nm)		$n_{s,m}$ (mmol g _{Pt} ⁻¹)	$D_{\text{Pt}} (-)$	d_{CO} (nm)	$S_{\text{CO-chem}}$ (m ² g _{Pt} ⁻¹)
X-Pt-2/450 [23]	2.7	2	0.7	2.5	2.7	0.07	1.53	0.48	2.3	122
H2-200-1	2.7	1.8	0.8	2.5	2.9	0.33	1.15	0.36	3.1	92
H2-350-3	2.8	1.8	0.8	2.5	2.7	0.23	1.48	0.46	2.4	118
H2-450-3	2.7	1.7	0.7	2.3	2.6	0.13	1.56	0.49	2.3	124
He-650-3	2.5	1.8	0.8	2.5	2.8	0.09	1.25	0.39	2.9	99
He-750-3	6.0	3.3 ^a	1.5 ^a	4.4 ^a	4.8 ^a	<d.l. ^b	0.38	0.12 ^c	9.4	30

d_{XRD} = average size of Pt particles estimated from X-ray line broadening; d_{TEM} = average size of Pt particles estimated from TEM; σ = standard deviation associated with d_{TEM} ; d_s = average surface diameter of Pt particles, $\sum n_i d_i^3 / \sum n_i d_i^2$, estimated from TEM; d_v = average volume diameter of metal particles, $\sum n_i d_i^4 / \sum n_i d_i^3$, estimated from TEM; Cl/Pt = surface Cl/Pt ratio measured by XPS; $n_{s,m}$ = amount of CO needed to form a chemisorbed monolayer on surface Pt atoms; D_{Pt} = metal dispersion; d_{CO} = equivalent average Pt particle diameter obtained from CO chemisorption; $S_{\text{CO-chem}}$ = accessible Pt surface deduced from CO chemisorption.

^a Not representative due to the bimodal distribution.

^b Below the detection limit, d.l.

^c Calculated supposing $X_{\text{Pt-CO}} = 1.61$: might be overestimated due to the presence of large particles for which one usually considers $X_{\text{Pt-CO}} = 1$.

electrode. This electrode (diameter = 5 mm) had been previously polished with diamond paste down to 1 μm and washed for 15 min in three successive ultrasonic baths of acetone, ethanol–water (1:1) and water. The aliquot was then dried and sintered for 15 min at 150 °C in air to reconstitute the Nafion® network and to ensure the binding of the AL to the glassy carbon surface. In order to remove the air contained in the AL and to fill its porosity with electrolyte solution, a drop of 1 M H₂SO₄ was deposited onto the catalyst, prior to outgassing under primary vacuum until no air bubbles were visible. All the experiments were carried out in 1 M sulphuric acid (Suprapur-Merck) at $T = 25$ °C, using an Autolab-PGSTAT20 potentiostat with a three-electrode cell and a saturated calomel electrode (SCE) as reference (+0.245 V vs. normal hydrogen electrode, NHE). However, all the potentials are expressed on the NHE scale hereafter. The SCE electrode was separated from the working electrode (WE) compartment via a Luggin capillary filled with 1 M H₂SO₄, therefore preventing any Cl[−] pollution of the electrolyte.

CO stripping measurements were performed as follows. The Pt surface was saturated with CO (N47, Alphagaz) by bubbling for 6 min in solution; afterwards, the non-adsorbed CO was removed from the cell by Ar bubbling for 39 min. During the CO adsorption and Ar bubbling, the electrode was held at +0.095 V vs. NHE. Voltammetric cycles were then recorded at 0.02 V s^{−1} between +0.045 and +1.245 V vs. NHE. Three consecutive cycles were recorded, and the specific surface area, $S_{\text{CO-strip}}$, was calculated from the charge required to electrooxidize the CO_{ads} monolayer and dividing by the mass of Pt loaded onto the glassy carbon disk. It was assumed that the electrooxidation of a CO_{ads} monolayer requires 420×10^{-6} C cm_{Pt}^{−2} [32].

In order to measure the electrocatalytic activity of the catalysts towards the ORR, the electrolyte solution was saturated with oxygen (O₂). During the measurement, the O₂ concentration was kept at saturation by gentle O₂-bubbling. The quasi-steady-state voltammograms were recorded at 10^{−3} V s^{−1} from +1.095 to +0.245 V vs. NHE. In order to account for diffusion–convection of the reactants in the electrolyte, the experiment was repeated at four RDE rotation speeds (42, 94, 168 and 262 rad s^{−1}) and the average mass-transport corrected intensity obtained from the four curves was used in the calculations [33]. To evaluate the catalyst activity towards the ORR, three parameters were isolated: (i) the Tafel slope, b , (ii) the specific activity at 0.85 V vs. NHE, SA₈₅, and (iii) the specific activity at 0.90 V vs. NHE, SA₉₀. These potentials correspond to 0.38 and 0.33 V ORR overpotentials in 1 M sulphuric acid, values classically monitored in a PEM fuel cell cathode at low current densities (i.e. under kinetic control).

In a regular experiment, six CO stripping experiments were first recorded, followed by ORR measurements in O₂-saturated 1 M H₂SO₄. A seventh CO stripping measurement was then performed to ensure that the electrochemically surface area (ECSA) did not change during the ORR measurements. The influence of repetitive CO stripping experiments was determined by measuring the ORR activity directly on the sample H2-350-3; the ECSA being determined after the kinetic measurements: this sample is referenced as H2-350-3/pre-CO. Finally, after electrochemical characterization, the catalysts were scrapped from the glassy carbon disk, and transferred onto a TEM grid to check whether the particle size distribution was modified.

2.5. Fuel cell tests

The catalyst H2-200-1 was tested at the cathode side of a PEM fuel cell and its performance was compared to that of the reference sample (X-Pt-2/450 [23]), reduced under H₂ for 5 h at $T = 450$ °C. All experimental conditions were kept identical for both catalysts. The samples were first used to prepare 50 cm² membrane electrode

assemblies (MEAs), which were then tested on a unit cell test bench. The MEA preparation method, the test device and the measurement procedure are completely described in Ref. [18]. Briefly, the MEAs were prepared by the decal method, which consists in spraying an ink composed of Pt/carbon catalyst, water and ionomer (Nafion®) onto a Kapton® sheet; afterwards, the electrolyte, i.e. a Nafion® membrane, and the anode (commercial, Paxitech), composed of a Pt-doped carbon black deposited onto a carbon felt, were piled up on the sprayed layer. The whole assembly was further hot-pressed to compose the MEA. The amount of catalyst was kept constant in the catalytic layer and the Nafion®/carbon mass ratio of the ink used to prepare the MEAs, N/C, was fixed at 0.5.

After a standardized start-up procedure, polarization curves, i.e. the $E_{\text{cell}} = f(i)$ curves, were measured by setting the cell voltage, E_{cell} , at each desired value for 15 min, which ensured the stabilization of the current density, i . Cyclic voltammetry measurements were performed *in situ* on the MEAs on the testing bench. The working electrode was the cathode fed with humidified nitrogen (100% relative humidity); the anode of the MEA was fed with humidified hydrogen (100% relative humidity) and was thus considered as both the reference electrode and the counter electrode. The voltammograms were monitored at 0.1 V s^{−1}, 0.05 V s^{−1} and 0.025 V s^{−1} between 0.06 V and 1 V with respect to the H₂-fed anode. The electrochemically active area, $A_{\text{Pt,MEA}}$, was determined by coulometry under hydrogen-desorption peaks in the third cycle, considering that 220×10^{-6} C correspond to 1 cm² of accessible Pt [16]. The average value of the Pt active area was calculated from experiments conducted at the various cycling speeds.

3. Results

3.1. Physico-chemical characterization of the catalysts

The TEM micrographs and the associated Pt particle size distributions of the synthesized catalysts are shown in Fig. 1. The average particle size, d_{TEM} , and its standard deviation, σ , are reported in Table 1, and compared to the data obtained on the reference material, X-Pt-2/450, taken from Ref. [23]. A key result of the study is that, except He-750-3, all the samples display homogeneously dispersed metal particles with an average size of 1.7–1.8 nm and a low standard deviation ($\sigma = 0.7$ –0.8 nm). This suggests no or slight metal aggregation for post-treatment temperatures up to 650 °C (Fig. 1f). At $T > 650$ °C, the Brownian motions of the Pt nanocrystallites cause their collision, aggregation and coalescence as suggested by the X-ray diffractograms presented in Fig. 2: the curves overlap up to $T = 450$ °C, and sharp peaks develop for $T > 650$ °C. The change is barely visible for sample He-650-3, but very pronounced for He-750-3; in parallel, the average crystallite size calculated from Scherrer's equation, d_{XRD} , increases from 2.5–2.7 nm ($T < 650$ °C) to 6.0 nm ($T > 650$ °C). The average crystallite size calculated by Scherrer's equation nicely compares with the volume weighted average diameter, $d_v = \sum n_i d_i^4 / \sum n_i d_i^3$, calculated from TEM images [30] for all the catalysts except for sample He-750-3 ($d_{\text{XRD}} = 6.0$ nm vs. $d_v = 4.8$ nm, Table 1). This nicely confirms the formation of larger crystallites at $T = 750$ °C (Fig. 1f). Finally, the reference sample, X-Pt-2/450, displays similar Pt particle size relative to samples post-treated at low temperature ($d_{\text{XRD}} = d_v = 2.7$ nm, Table 1).

XPS measurements show that the Cl/Pt ratio decreases regularly from 0.33 (H2-200-1) to 0.09 (He-650-3) when the duration or the temperature of the post-treatment increase (Table 1). In the case of sample He-750-3, the amount of chlorine was below the detection limit (Cl/Pt ~ 0.05) and could not be quantified. Fig. 3 shows the

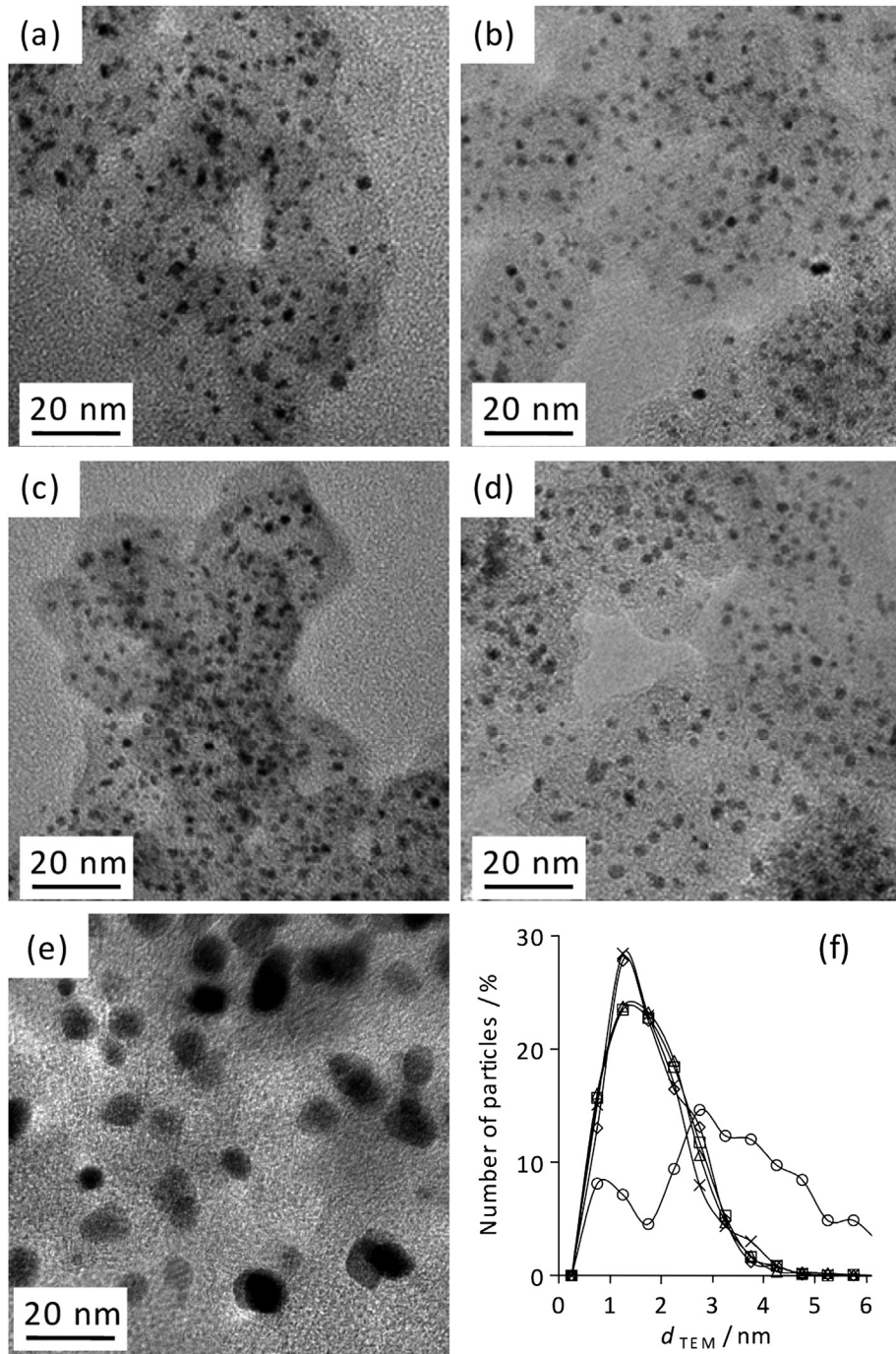


Fig. 1. TEM analysis. TEM micrographs of samples H2-200-1 (a), H2-350-3 (b), H2-450-3 (c), He-650-3 (d) and He-750-3 (e). Pt particle size distribution determined from image analysis (f): H2-200-1 (x), H2-350-3 (◇), H2-450-3 (◻), He-650-3 (△) and He-750-3 (○).

XPS spectrum for H2-200-1, *i.e.* the sample most contaminated with Cl. The general spectrum displays the expected strong C1s contribution at 284.8 eV together with O1s at 533 eV. A small peak attributable to Pt4f is observed at 72 eV. The chlorine peak at 200 eV is barely visible but is nevertheless present and becomes quantifiable by scans accumulation in that particular region. The inset shows the Cl_{2p} peak used to calculate the Cl/Pt ratio: the signal to noise ratio is very low, and induces some incertitude on the Cl/Pt ratio (20–30%). The XPS data measured on the reference sample (X-Pt-2/450, Ref. [23]) are in line with those of the present study: indeed, the Cl/Pt ratio equals 0.07 for a post-treatment under H₂ at 450 °C during 5 h.

Table 1 also gathers the data derived from CO chemisorption. The amount of CO needed to form a chemisorbed monolayer on surface Pt atoms, $n_{s,m}$, first increases with the post-treatment temperature, from 1.15 mmol g_{Pt}⁻¹ (H2-200-1) to 1.56 mmol g_{Pt}⁻¹ (H2-450-3), then decreases to 0.38 mmol g_{Pt}⁻¹ (He-750-3). From $n_{s,m}$, the Pt dispersion, *i.e.* the proportion of available Pt surface atoms, can be calculated by [30]:

$$D_{Pt} = n_{s,m} M_{Pt} X_{Pt-CO} \times 10^{-3} \quad (1)$$

where M_{Pt} is the atomic weight of Pt (195.09 g mol⁻¹) and X_{Pt-CO} represents the chemisorption average stoichiometry, *i.e.* the average number of Pt atoms on which one CO molecule is adsorbed. In the

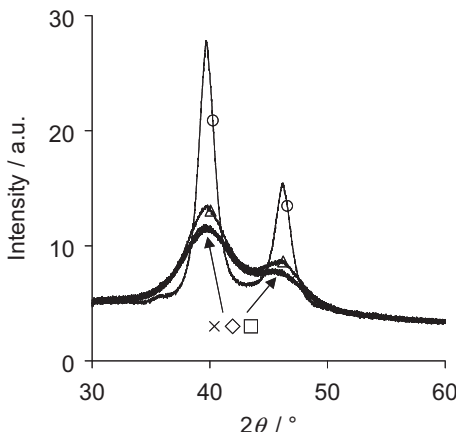


Fig. 2. X-ray diffractograms of catalysts H2-200-1 (x), H2-350-3 (◇), H2-450-3 (□), He-650-3 (△) and He-750-3 (○).

present study, $X_{\text{Pt}-\text{CO}}$ was chosen equal to 1.61 (i.e. considering a mix between linear and bridged bonding), following the results obtained by Rodríguez-Reinoso et al. in the case of Pt particles smaller than 5 nm [34]. As a consequence of the evolution of $n_{s,m}$, the corresponding Pt dispersion, D_{Pt} , passes through a maximum for sample H2-450-3 ($D_{\text{Pt}} = 0.49$) a value which is almost equal to that obtained for the reference sample X-Pt-2/450 ($D_{\text{Pt}} = 0.48$) and very close to that of H2-350-3 ($D_{\text{Pt}} = 0.46$). For samples He-650-3 and He-750-3, D_{Pt} drops to 0.39 and 0.12, respectively confirming aggregation of the Pt nanoparticles above $T = 650$ °C.

From D_{Pt} , the ‘average equivalent particle diameter’, d_{CO} , was calculated. d_{CO} represents the particle diameter leading to a metal surface equivalent to that detected by chemisorption [30]:

$$d_{\text{CO}} = \frac{6(v_m/a_m)}{D_{\text{Pt}}} \quad (2)$$

where v_m is the average volume occupied by a metal atom in the bulk of a metal particle (for Pt: $v_m = 0.0151$ nm³) and a_m is the average surface area occupied by a surface metal atom (for Pt: $a_m = 0.0807$ nm²) [30]. Since chemisorption is a surface-sensitive phenomenon, d_{CO} should be compared to a surface-weighted

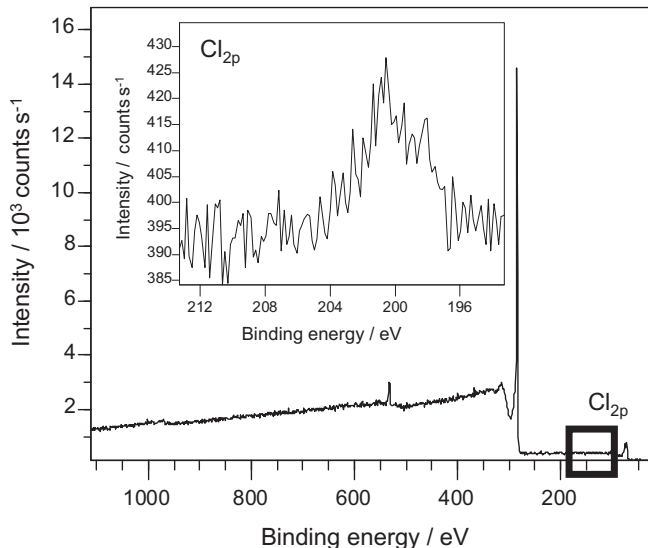


Fig. 3. Example of XPS results: spectrum obtained with sample H2-200-1, presenting the highest chlorine content.

average diameter, d_s [30]. **Table 1** shows that the values of d_{CO} and d_s compare well except for sample He-750-3 ($d_{\text{CO}} = 9.4$ nm; $d_s = 4.4$ nm); this likely arises from the bimodal particle size distribution with large tailing on the large diameter side of the histogram, which was not taken into account for the estimation of d_s . Finally, assuming that the particles are spherical, the Pt surface available for catalysis can be calculated from d_{CO} and the density of Pt, ρ_{Pt} (21.09 g cm⁻³). Indeed:

$$S_{\text{CO-chem}} = 6 \frac{V_{\text{Pt}}}{d_{\text{CO}} m_{\text{Pt}}} = 6 \frac{1}{d_{\text{CO}} \rho_{\text{Pt}}} \quad (3)$$

where V_{Pt} and m_{Pt} are the volume and the mass of Pt present in the catalyst, respectively. The results gathered in **Table 1** show that the detected surface first increases from 92 m² g_{Pt}⁻¹ (H2-200-1) to 124 m² g_{Pt}⁻¹ (H2-450-3), then decreases to 99 m² g_{Pt}⁻¹ (He-650-3) and 30 m² g_{Pt}⁻¹ (He-750-3). The Pt surface obtained for the reference sample (X-Pt-2/450) nearly equals that of sample H2-450-3 (122 and 124 m² g_{Pt}⁻¹, respectively).

3.2. Electrochemical characterization

Table 2 gathers the main electrochemical characterization results for the synthesized catalysts. The specific surface area calculated from the coulometry of the first CO stripping measurement, $S_{\text{CO-strip}}(1)$, increases from 37 to 90 m² g_{Pt}⁻¹ when increasing the post-treatment temperature from 200 to 450 °C. For temperatures above 450 °C, the values of $S_{\text{CO-strip}}(1)$ decrease to 57 m² g_{Pt}⁻¹ (He-650-3) and to 20 m² g_{Pt}⁻¹ (He-750-3), which reflects the aggregation-coalescence of the Pt nanoparticles under these conditions. **Fig. 4a** shows representative background-subtracted CO stripping voltammograms obtained on each catalyst. It is interesting to note that the position of the main electrooxidation peak shifts towards lower potential values when the post-treatment temperature increases from 200 °C (H2-200-1: +0.99 V vs. NHE) to 450 °C (H2-450-3: +0.93 V vs. NHE). At $T = 650$ °C, a pre-peak appears at around +0.82 V vs. NHE (He-650-3) and the potential value of the main peak continues to decrease (He-650-3: +0.92 V vs. NHE). In the case of sample He-750-3, the charge under the pre-peak develops at

Table 2
Electrochemical characterization of the catalysts.

Sample	CO stripping			ORR	
	$S_{\text{CO-strip}}(1)$ (m ² g _{Pt} ⁻¹)	$S_{\text{CO-strip}}(7)$ (m ² g _{Pt} ⁻¹)	b (V dec ⁻¹)	SA ₈₅ (μA cm _{Pt} ⁻²)	SA ₉₀ (μA cm _{Pt} ⁻²)
	±10%	±10%	±5%	±5%	±5%
X-Pt-2/450 [23]	127	142	-0.066	56	12
H2-200-1	37	69	-0.074	41	10
H2-350-3	61	87	-0.070	48	11
H2-450-3	90	106	-0.068	55	12
He-650-3	57	80	-0.067	57	11
He-750-3	20	21	-0.076	53	12
H2-350-3/pre-CO	78	—	-0.069	43	10

$S_{\text{CO-strip}}(1)$: Pt surface area determined using the coulometry of the first CO_{ads} stripping experiment; $S_{\text{CO-strip}}(7)$: Pt surface area determined using the coulometry of the seventh CO_{ads} stripping experiment; b : Tafel slope for the oxygen reduction reaction (ORR); SA₈₅ = specific activity at $E = 0.85$ V; SA₉₀ = specific activity at $E = 0.90$ V.

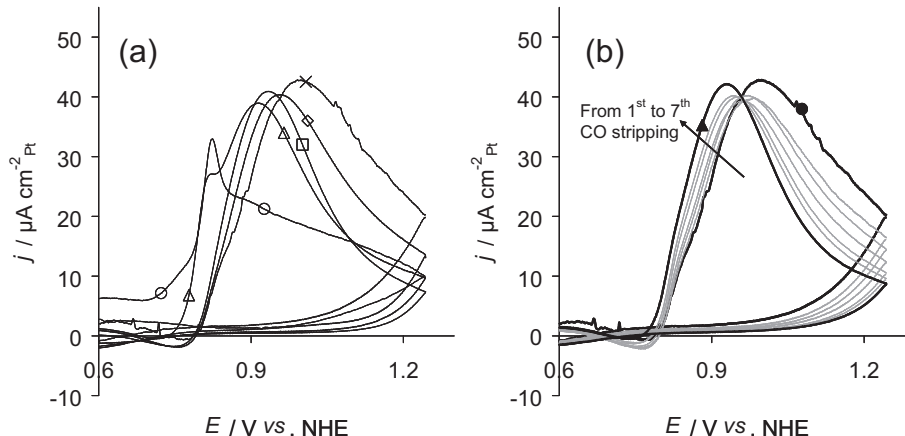


Fig. 4. CO_{ads} stripping voltammogram in H_2SO_4 (1 M) at 25°C ; sweep rate of 0.02 V s^{-1} . (a) First CO stripping obtained on the five catalysts: H2-200-1 (\times), H2-350-3 (\diamond), H2-450-3 (\square), He-650-3 (\triangle) and He-750-3 (\circ); (b) 7 successive CO strippings performed on the sample presenting the highest chlorine content (H2-200-1): 1st CO stripping (\bullet), 7th CO stripping (\blacktriangle), the grey curves represent the intermediate cycles, from 2nd to 6th.

the expense of the main peak (located below 0.9 V vs. NHE). Fig. 4b displays seven consecutive CO stripping voltammograms performed on sample H2-200-1, i.e. the catalyst presenting the highest chlorine content ($\text{Cl}/\text{Pt} = 0.33$). Each CO stripping voltammogram is normalized to the electrochemically active surface area measured on this cycle: the position of the main electrooxidation peak shifts towards lower potential values, e.g. from $+0.99 \text{ V}$ vs. NHE (1st CO stripping) to $+0.92 \text{ V}$ vs. NHE (7th CO stripping).

Fig. 5a shows an example of ORR measurements voltammograms obtained on sample H2-350-3 for four rotating speeds, i.e. 400, 900, 1600 and 2500 rpm. The kinetic current density, i_k , which includes the correction for the diffusion in the liquid electrolyte, was calculated from Ref. [33]:

$$i_k = \frac{i i_l}{i_l - i} \quad (4)$$

where i is the measured current density and i_l is the limiting current density. The Tafel plots (i.e. E vs. $\log(i_k)$) are presented in Fig. 5b. The ORR curves are nearly superimposed in the potential range $0.85 < E < 0.92 \text{ V}$. Slightly better ORR specific activities are nevertheless monitored for the samples that have undergone a

higher H_2PtCl_6 precursor reduction temperature; the effect being more evident for the He-750-3 sample (Table 1). This is believed to result from the larger crystallite size of this sample (the ORR kinetics are size dependent, see Refs. [35,36]). The Tafel slope for the ORR, b , was calculated by fitting the Tafel plots between $+0.95$ and $+0.80 \text{ V}$ vs. NHE, and ranges from -0.066 to $-0.076 \text{ V dec}^{-1}$ (Table 2), close to the $-0.060 \text{ V dec}^{-1}$ value that is classically reported for Pt/C nanoparticles [37,38]. The specific activities (SA) were calculated at $E = 0.85$ or 0.90 V vs. NHE by normalizing i_k to the electrochemically active Pt surface area measured from the CO_{ads} stripping coulometry. Since the ORR measurements were performed after six CO stripping sequences, the Pt surface area considered is the average between the surface areas obtained for the 6th and 7th CO stripping measurements. Note however that the difference between the two surface areas is usually low (<5%). The specific activities measured at $E = 0.90 \text{ V}$ vs. NHE, SA_{90} , are nearly independent of the tested catalyst ($10\text{--}12 \mu\text{A cm}^{-2}$). However, they strongly differ at $E = 0.85 \text{ V}$ vs. NHE (SA_{85}), smaller values being monitored for the more poisoned electrocatalysts: H2-200-1 ($41 \mu\text{A cm}^{-2}$), H2-350-3 ($48 \mu\text{A cm}^{-2}$) relative to the other catalysts ($53\text{--}57 \mu\text{A cm}^{-2}$).

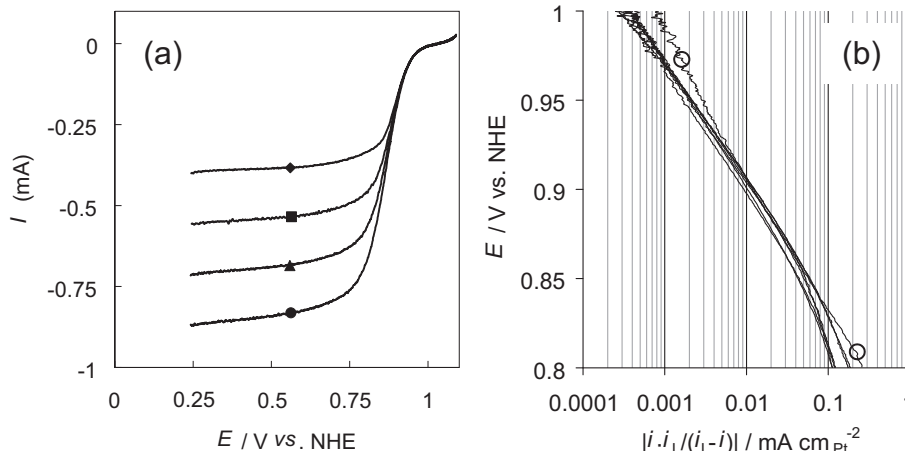


Fig. 5. (a) Example of ORR measurements in O_2 -saturated 1 M H_2SO_4 at 25°C , sweep rate of 10^{-3} V s^{-1} , rotating speed of 400 rpm (\blacklozenge), 900 rpm (\blacksquare), 1600 rpm (\blacktriangle) and 2500 rpm (\bullet), sample H2-350-3. (b) Tafel representation of the ORR voltammograms: voltage as a function of the current density corrected from the diffusion-convection in the solution. Except for He-750-3 (\circ), the curves are not labelled because of superimposition.

It is important to note that subsequent CO stripping procedures do not affect much the intrinsic specific activity (*i.e.* ratioed to the active area of Pt) of the catalysts. Indeed, Table 2 shows that the values of SA₈₅ and SA₉₀ are similar on the fresh H2-350-3 sample (H2-350-3/pre-CO) or after six consecutive CO stripping sequences (H2-350-3). This is not due to a change of the Pt particle size as evidenced by the particle size distribution established before/after the electrochemical measurements (not shown).

3.3. Fuel cell tests

The polarization curves, *i.e.* the $E_{\text{cell}} = f(i)$ curves, of MEAs prepared with catalysts H2-200-1 and X-Pt-2/450 are presented in Fig. 6a. The mass current density, j_m , increases from about 0.1 to 0.7 kA g_{Pt}⁻¹ at $E = 0.6$ V vs. NHE, and from about 2.2 to 6.7 kA g_{Pt}⁻¹ at $E = 0.2$ V vs. NHE after an increase of the reduction temperature from 200 to 450 °C. Since the intrinsic specific activity of the accessible Pt atoms is comparable for all the electrocatalysts (see Section 3.2), this result indicates that the metal atoms are much more efficiently utilized in the MEA prepared using X-Pt-2/450 than in the MEA processed with catalyst H2-200-1. The result is confirmed by the cyclic voltammograms performed *in situ* on the same MEAs (Fig. 6b). Indeed, the features associated with H or O adsorption/desorption on/from Pt are weakly marked for the MEA prepared with H2-200-1 compared to those obtained with X-Pt-2/450. This translates into specific surface areas, $A_{\text{Pt,MEA}}$, equal to 14–64 m² g_{Pt}⁻¹, respectively (Table 3), for identical Pt loading at the cathode (0.13 and 0.12 mg_{Pt} cm⁻²).

4. Discussion

4.1. Estimation of the real surface area

The results presented in this study underline very clearly the importance of the technique used for determining the electrochemically active surface area of Pt/C nanoparticles. It is striking to note that the specific surface areas measured by CO chemisorption in the gas phase or in the liquid phase (CO stripping) are not equivalent, while the principle of both techniques is similar: in both cases, the Pt surface is estimated from the amount of CO chemisorbed on the particles (Tables 1 and 2). Such differences can be correlated with the presence of Cl⁻ ions issued from the incomplete decomposition/removal of the chloride-based Pt salt used as

Table 3
Characteristics of the cathodes and Pt utilization ratios.

Catalyst	Pt _{load} (mg _{Pt} cm ⁻²)	$A_{\text{Pt,MEA}}$ (m ² g _{Pt} ⁻¹)	u_{Pt} (-)
H2-200-1	0.13	14	0.38
X-Pt-2/450 [23]	0.12	64	0.50

Pt_{load} = platinum loading of the cathode; $A_{\text{Pt,MEA}}$ = specific surface area of Pt in the cathode of the MEA, detected by *in situ* cyclic voltammetry; u_{Pt} = Pt particle utilization ratio in the cathode of the MEA.

precursor of the Pt nanoparticles. In addition, consecutive CO stripping measurements performed on a poisoned sample (H2-200-1) show that the detected Pt surface area increases with the number of CO stripping experiments (Table 2) while no Pt particle size modification is observed: this suggests that the Cl⁻ atoms adsorbed at the Pt surface are gradually displaced by CO molecules in the liquid electrolyte. Consequently, the electrochemically active Pt surface area used in ORR catalysis is systematically overestimated because the two surface area measurement methods induce Cl⁻ depoisoning. Furthermore, the displacement of Cl⁻ ions is not complete, which causes large incertitude in the estimation of the real surface area by both techniques. This is illustrated in Fig. 7, where the Pt specific surface areas measured by CO chemisorption in the gas phase and in the liquid phase are compared. Fig. 7a displays the variations of $S_{\text{CO-chem}}$ vs. the Cl/Pt ratio. The surface area is almost constant for samples H2-350-3, H2-450-3 and X-Pt-2/450, while the Cl/Pt ratio decreases from 0.23 to 0.07; the detected surface area is lower for samples H2-200-1 and He-650-3; in the latter case, the decrease of Pt surface area can be explained by the fact that Pt particle sintering initiates close to 650 °C. On the contrary, in Fig. 7b, the $S_{\text{CO-strip}}(1)$ vs. Cl/Pt plot is linear for samples displaying the same Pt particle size, *i.e.* H2-200-1, H2-350-3, H2-450-3 and X-Pt-2/450. In the case of He-650-3, which does not fit in the linear relationship, the decrease of the Pt surface area, $S_{\text{CO-strip}}(1)$ was previously rationalized by the observed aggregation-coalescence of the Pt nanocrystallites, as shown by the existence of the pre-peak at +0.82 V vs. NHE (Fig. 4a) in CO_{ads} stripping experiments. Indeed, it is well-established that the presence of Pt nanoparticles featuring surface defects, such as Pt aggregates, yields a CO_{ads} electrooxidation pre-peak, which is shifted towards negative potential vs. the main peak [39–42].

For all catalysts except X-Pt-2/450, the values of specific surface area calculated from gas-phase CO chemisorption are higher than

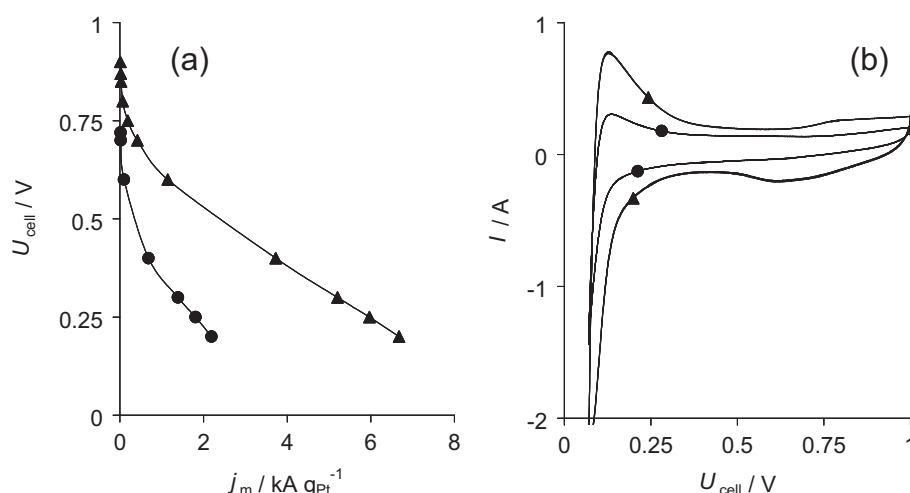


Fig. 6. PEM fuel cell tests performed on Membrane-Electrode Assemblies with cathode processed using (●) H2-200-1 and (▲) X-Pt-2/450 [23], *i.e.* the reference sample reduced at 450 °C under H₂ during 5 h. (a) Polarization curves at 70 °C; (b) cyclic voltammetry performed *in situ* on the same MEAs, sweep rate of 0.1 V s⁻¹.

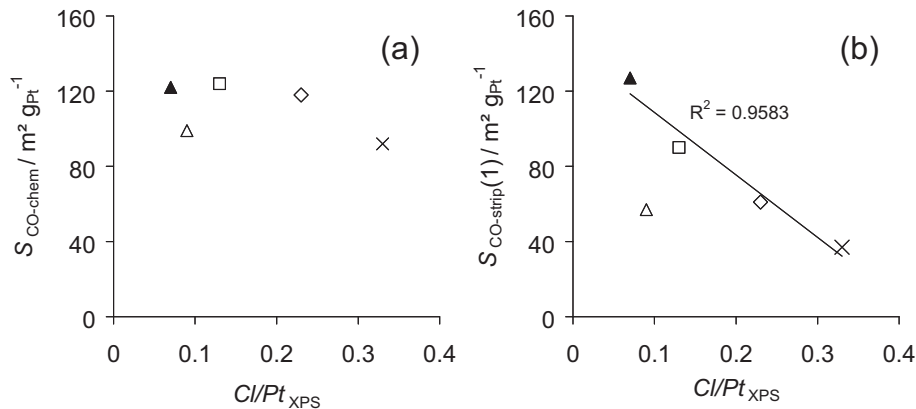


Fig. 7. Relationship between the chlorine content and (a) the Pt surface detected by CO chemisorption or (b) the Pt surface detected by CO stripping (first measurement of the seven-cycle series). H2-200-1 (x), H2-350-3 (◇), H2-450-3 (□), He-650-3 (△) and X-Pt-2/450 (▲) [23]. Sample He-750-3 is omitted because the amount of Cl present in the sample is below the XPS detection limit.

those obtained by CO stripping, even after a series of seven experiments. This can be rationalized by considering different CO activity and duration of the adsorption step in each technique. In the gas-phase, the adsorption equilibrium must be reached before any additional CO is injected in the measurement cell. Such experimental conditions yield desorption of the Cl^- ions from the Pt surface; $S_{CO\text{-chem}}$ is thus not representative of the true Pt surface area available for electrocatalysis, or in other words, $S_{CO\text{-chem}}$ reflects the maximum Pt surface area that could be available for electrocatalysis, if the Pt/C catalyst was chloride-free; this latter comment may not hold completely true for H2-200-1, the catalyst that exhibits the highest level of Cl pollution. On the contrary, $S_{CO\text{-strip}(1)}$ is directly linked to the amount of chlorine species detected by XPS in the sample. These results underline the importance of the technique used for determining surface area as well as the possible influence of this technique on the final surface reactivity of the Pt/C catalyst. Last but not least, it is worth noting that the ORR kinetics measurements also induce the “cleaning” of the Pt particles, as shown by the comparison of the Pt surface areas obtained by CO stripping before and after kinetics measurements: indeed, sample H2-350-3 and H2-350-3/pre-CO display Pt surface areas, $S_{CO\text{-strip}(1)}$, equal to 61 and $78 m^2 g_{Pt}^{-1}$, respectively.

Summing up, the results presented in this study clearly show that Pt nanoparticles synthesized from a chloride-containing Pt precursor are contaminated with Cl^- ions adsorbed at their surface. The content of Cl^- ions at the surface can be varied by monitoring the temperature and the duration of the reduction step. Note that the effect of chlorine poisoning on the performance of Pt/C and PEMFC was previously observed, for instance by contacting the catalyst with the poison or by adding CCl_4 to the gas feeding stream of the fuel cell [43,44]. Although the source of Cl leading to poisoning was different, the results obtained showed a similar decrease of the metal surface area of Pt/carbon black catalysts in the presence of CCl_4 in H_2 stream.

4.2. Effect of Cl^- poisoning on PEM fuel cell reaction kinetics

This study provides clear evidences that chloride-based Pt precursors used for the synthesis of Pt nanoparticles strongly affect the surface reactivity and the electrocatalytic activity of PEM fuel cell catalytic layers.

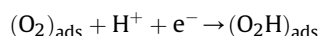
In the potential region $0.05 < E < 0.40$ V vs. NHE, where hydrogen atoms are underpotentially deposited (H_{upd}), an increase of the Cl/Pt ratio causes the H_{upd} peaks to disappear at the benefit of a single peak at $E = 0.12$ – 0.13 V vs. NHE (Fig. 4a). This

suggests that Cl^- ions are specifically adsorbed on the Pt surface even at low potential, in agreement with previous studies on polycrystalline Pt [45,46] or carbon-supported Pt nanoparticles [47,48]. It has been suggested from studies on Pt single crystals that the adsorption of Cl^- ions blocks the (111) [48] and (100) facets of the Pt/C nanoparticles [47,49] and changes the adsorption energy of the neighbouring adsorption sites [47]. Above the potential of zero total charge, the adsorption of Cl^- ions shifts positive and hinders the surface oxide formation. The latter directly impacts the kinetics of the CO_{ads} electrooxidation (Fig. 4a). Indeed, CO_{ads} electrooxidation proceeds via a Langmuir–Hinshelwood mechanism on Pt, which includes water dissociation into oxygen-containing species, and recombination of the former species with CO, yielding CO_2 [38–41]. The shift towards higher potential values of the main peak in CO_{ads} stripping experiments suggests that water and chloride species compete for the Pt catalytic sites [39,41,42]. Indeed, with an increase of the Cl/Pt ratio from 0.13 (H2-450-3) to 0.33 (H2-200-1), the CO_{ads} electrooxidation peak position is shifted from +0.93 to +0.99 V vs. NHE, respectively, and the electroactive area ($S_{CO\text{-strip}(1)}$) decreases from 90 to $37 m^2 g_{Pt}^{-1}$. Since the particle size distribution is nearly identical for these three samples, any effect of the particle size on the CO_{ads} electrooxidation kinetics can be ruled out [39–42]. A closer look at Fig. 4a indicates that the shift of the main electrooxidation peak mainly arises from the stronger asymmetry of the ascending part of the voltammogram (i.e. before the main peak) but, surprisingly, water splitting (OH_{ads} formation) is not inhibited on chloride-poisoned surfaces, as shown by the similar onsets of the reaction on H2-200-1, H2-350-3 and H2-450-3. It is therefore concluded (i) that some sites on which OH_{ads} are formed are not poisoned by Cl^- ions and (ii) that the reaction rate is limited by $CO_{ads} + OH_{ads}$ recombination before the main current peak. Interestingly, the asymmetry of the CO_{ads} stripping voltammograms is more pronounced after the current maximum (i.e. at a potential above that of the main CO_{ads} electrooxidation peak). Similar changes were previously observed on Pt nanoparticles with a size $d < 3$ nm, and rationalized in terms of decreased CO_{ads} surface mobility [39–42]. Similarly, in this work, it may be inferred that the increasing Pt– Cl_{ads} interaction at high electrode potential decreases the mobility of CO_{ads} molecules towards the sites where OH_{ads} species are nucleated.

The poisoning of the Pt surface by Cl^- ions is also confirmed by results of Fig. 4b. Although the analysis of representative TEM images show no change of the Pt nanoparticle size, the CO_{ads} electrooxidation peak is shifted towards lower potential values and the

peak asymmetry decreases as consecutive CO stripping procedures are performed on sample H2-200-1. Simultaneously, the Pt specific surface area, $S_{CO\text{-strip}}$, increases from 37 to 69 $\text{m}^2 \text{ g}_{\text{Pt}}^{-1}$ (Table 2). Since CO is strongly adsorbed onto Pt [50], it is suggested that successive CO stripping procedures facilitate the desorption of Cl^- ions, and cause an increase of the electroactive Pt surface area. Nevertheless, the slow desorption kinetics of Cl^- ions do not enable complete Pt surface cleaning, even after seven CO stripping procedures. Note that, in the case of electrocatalysis in fuel cell, the cleaning of the catalyst is improbable except in the presence of excess water. Catalyst cleaning was however observed at low cell voltages by Martínez-Rodríguez et al. [43] and Zhang et al. [44] after poisoning the anode with CCl_4 : the performance recovery was obtained under low potential conditions, i.e. at high current density, or by purging the cathode with inert gas or hydrogen.

Similarly to what was observed for the electrochemical CO_{ads} oxidation, the ORR kinetics is depreciated in the presence of Cl^- ions: decreased specific activity (Tables 2 and 3 and Fig. 5b) and decreased PEM fuel cell performance are monitored for chloride-poisoned Pt/XC surfaces in the low current density region of the polarization curve (Fig. 6a). Such changes agree with previous findings of Durand et al. [51] on Pt(111) single crystals and from Schmidt et al. [47] on Pt/C nanoparticles. They can be accounted for by considering the rate determining step of the ORR [52]:



The ORR rate can be expressed as:

$$j_k = -nFkC_{\text{O}_2} [\text{H}^+] (1 - \theta_{\text{ads}})^x \exp \frac{-\alpha FE}{RT} \exp \frac{\Delta G_{\theta_{\text{ads}}}^\#}{RT} \quad (5)$$

where n is the number of exchanged electrons, k is the rate constant of the rate determining step (i.e. the first proton and electron transfer), C_{O_2} is the surface concentration in adsorbed dioxygen, proportional to the partial pressure in O_2 , $[\text{H}^+]$ is the concentration of protons near the electrode surface, θ_{ads} is the total coverage by adsorbed species on the modified surface (dioxygen molecules, reaction intermediates, anions and surface oxides issued from water splitting), x is the number of sites occupied by the $(\text{O}_2\text{H})_{\text{ads}}$ adsorbate ($x = 1$ or 2), α is the charge transfer coefficient of the ORR, F is the Faraday constant, E is the electrode potential, $\Delta G_{\theta_{\text{ads}}}^\#$ is the coverage-dependent Gibbs free energy of the reaction and R and T have their usual meaning.

Eq. (5) forecasts that Cl^- ions modify the ORR kinetic current in two ways. First, they reduce the number of free Pt surface sites, available for the adsorption of O_2 molecules (the pre-exponential term $(1 - \theta_{\text{OH,ads}})^x$ in Eq. (5)). A likely proof for that is displayed in Fig. 8 showing a linear relationship between the $(1 - \text{Cl}/\text{Pt})$ ratio (i.e. the number of free Pt sites available for the adsorption of O_2 molecules and oxygen-containing ORR intermediates) and the kinetic current measured at $E = 0.85$ V vs. NHE. The only slight deviation from this straight line is observed for X-Pt-2/450, a sample issued from another batch. Note that the linear relationship passes through the origin (0,0), which hints at a 1:1 stoichiometry for the Pt:Cl bond. Second, in addition to a site-blocking effect, the Cl^- anions are believed to modify the Gibbs free energy of oxygen adsorption ($\Delta G_{\theta_{\text{ads}}}^\#$ in Eq. (5)) through repulsions between adsorbed anions and dioxygen molecules or oxygen-containing reaction intermediates [53]. Finally, it has been shown that Cl^- ions modify the ORR mechanism by enhancing the formation of H_2O_2 , i.e. in reducing the number of pairs that are required to break the O–O bond [47]: this translates into a slight but non-negligible increase of Tafel slope absolute values with the level of Cl-pollution (Table 2).

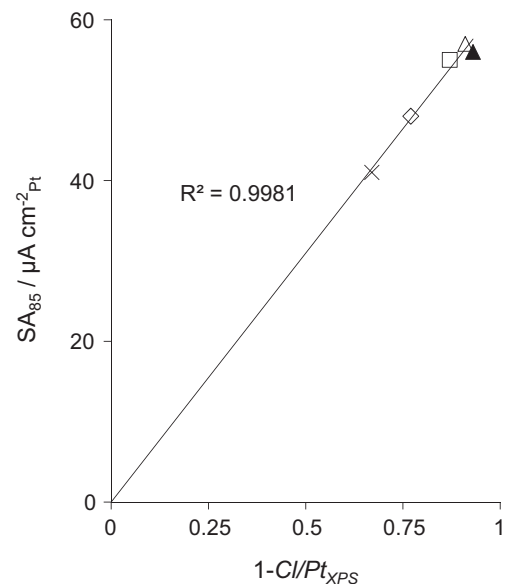


Fig. 8. Specific activity of Pt/C catalysts for the ORR at 25 °C (reported at $E = 0.85$ V vs. NHE) vs. the total coverage by surface-blocking species. Electrolyte: 1 M H_2SO_4 ; sweep rate of 1 mV s^{-1} . H2-200-1 (x), H2-350-3 (◇), H2-450-3 (□), He-650-3 (△) and X-Pt-2/450 (▲) [23]. Sample He-750-3 is omitted because the amount of Cl present in the sample is below the XPS detection limit.

We now discuss the results obtained in solid electrolyte, i.e. for real PEM fuel cell cathodes. The presence of Cl^- ions in the catalytic layer clearly decreases its performance in the low current density region (Fig. 6), where the ORR kinetics controls the PEM fuel cell performance. This loss of performance is accounted for by both the decreased electrochemically active Pt surface area and the decreased intrinsic catalytic activity of chloride-poisoned Pt surfaces. For instance, at a cell voltage of 0.6 V, the current density is divided by 7, dropping from 0.1 to 0.7 $\text{kA g}_{\text{Pt}}^{-1}$ (Fig. 6) as the Cl/Pt ratio increases from 0.07 to 0.33. It is interesting to note that a somewhat smaller decrease (i.e. current density divided by ~4.7) was expected on the basis of the experiments performed in liquid electrolyte reflecting a possible influence of Cl^- presence on the Nafion®/Pt contact.

Table 3 compares experimental values of the specific surface area determined by integration of the H_{upd} desorption charge, after subtraction of the currents originating from the carbon support, in solid polymer electrolyte, $A_{\text{Pt,MEA}}$ for both the X-Pt-2/450 and H2-200-1 samples. From these values, the Pt utilization factor, u_{Pt} , was calculated as the ratio between the active Pt surface area in the cathode, $A_{\text{Pt,MEA}}$, and the electroactive Pt surface area detected *ex situ* by CO stripping [11]. If one considers that the catalyst presents a homogeneous particle size distribution and that the cathodic catalytic layer is fully accessible to the reactants, u_{Pt} represents the fraction of Pt particles connected to both the membrane and the carbon support. For the calculation of u_{Pt} , the CO stripping measurement considered here is the first CO stripping surface, $S_{\text{CO-strip}}(1)$; indeed, the catalyst did not undergo any Cl^- removal before implementation in the MEA cathode. Table 3 shows that u_{Pt} increases from 0.38 to 0.50 when increasing the temperature and the duration of the reduction step from 200 to 450 °C and from 1 h to 5 h, respectively. This suggests that the presence of relatively large amounts of Cl^- ions at the surface of the Pt particles could be detrimental to the contact between Pt and Nafion®. This phenomenon could be caused by repulsive interactions between Cl^- ions adsorbed at the Pt surface and the Nafion® SO_3^- end chains, both negatively charged, which would hamper the catalyst

impregnation with Nafion® oligomers during the preparation of the ink. However, additional measurements would be necessary to confirm this hypothesis. Another effect that could explain the difference between liquid electrolyte and solid electrolyte systems is that, in the case of solid electrolyte, Cl⁻ ions are probably forced to remain close to the Pt particles due to the absence of excess water; on the contrary, in the case of liquid electrolyte, Cl⁻ ions are free to diffuse in the measurement cell.

4.3. Strategies to remove Cl⁻ ions

TEM micrographs and analysis performed in this study, as well as XRD measurements show that the Pt particle size does not change when increasing the temperature and duration of the reduction treatment under hydrogen up to $T = 450$ °C and 5 h, respectively. In parallel, the chlorine content of the catalyst measured by XPS decreases, while the Pt surface area detected by CO chemisorption increases up to a maximum of $124 \text{ m}^2 \text{ g}_{\text{Pt}}^{-1}$, which corresponds to Pt particle size around 2.3 nm. This strongly suggests that the reduction treatment performed at $T = 200$ °C under H₂ atmosphere is not sufficient to obtain clean Pt surfaces; higher temperatures and longer duration of reduction treatments are necessary to remove chlorine atoms from the surface of the Pt particles. The reduction temperature can be increased up to $T = 450$ °C without any damage to the metal distribution: no sintering is observed, which denotes a very good thermal stability of the Pt nanoparticles. However, since higher temperatures lead to the gasification of the carbon support, the reduction treatment must be long enough to eliminate chlorine from the catalyst: even after 5 h at 450 °C under pure hydrogen, traces of Cl⁻ ions are still observed (X-Pt-2/450: Cl/Pt = 0.07).

Conversely, thermal treatments under inert gas at temperatures higher than 450 °C can achieve better cleaning of the catalytic surface. However, a decrease of the Pt surface area measured by CO chemisorption, $S_{\text{CO-chem}}$, is observed: at $T = 650$ °C, the detected surface area equals $99 \text{ m}^2 \text{ g}_{\text{Pt}}^{-1}$ and drops to $30 \text{ m}^2 \text{ g}_{\text{Pt}}^{-1}$ at $T = 750$ °C. Although no increase of the particle size is detected by TEM image analysis or XRD at $T = 650$ °C, the Pt particle size distribution clearly moves to larger values when increasing the temperature to 750 °C (Fig. 1e and f). Pt particles sintering probably begins at temperatures around 600–650 °C, but remains relatively slow, while it becomes quite significant when increasing the temperature to 750 °C.

Since long reduction treatments at high temperature are necessary to remove all the chlorine from the Pt/C catalysts prepared from H₂PtCl₆ precursor, the best way to achieve Cl⁻ free catalysts with high efficiency in PEM fuel cell is certainly to avoid chlorinated precursors at the impregnation stage of the catalyst preparation.

5. Conclusions

A Pt/carbon xerogel catalyst with 2 nm Pt particles designed for PEM fuel cell electrodes was prepared by impregnation with H₂PtCl₆ using the Strong Electrostatic Adsorption (SEA) method. It was shown that the MEA performance increases largely with the reduction temperature and duration. This is rationalized by the partial blocking of the catalytic sites by residual Cl⁻ atoms issued from the incomplete decomposition of the metal precursor when the reduction treatment is not performed at sufficiently high temperature for sufficient duration. Increasing the reduction temperature and duration allows better cleaning of the Pt surface and improves the electrocatalytic performance.

The effect of chlorine poisoning was investigated on two model reactions of interest for PEM fuel cell electrocatalysis: the

electrochemical CO_{ads} oxidation and the ORR. The Cl⁻ ions strongly deprecate the CO_{ads} electrooxidation kinetics. At the onset of the reaction (below the main oxidation peak in CO_{ads} stripping voltammograms), the Cl⁻ ions limit the rate of the CO_{ads} + OH_{ads} recombination, whereas the CO_{ads} diffusion to the active sites, where OH is adsorbed, is strongly inhibited above the current maximum. The presence of adsorbed Cl⁻ species deprecates the ORR kinetics in three ways. First, they reduce the number of free Pt surface sites, available for the adsorption of dioxygen molecules and oxygen-containing reaction intermediates. Second, they possibly modify the Gibbs free energy of oxygen adsorption by causing repulsive interactions with the adsorbed oxygen-containing reaction intermediates. Finally, in solid electrolyte, the Cl⁻ ions are believed to be detrimental to the formation of the Pt/Nafion® contact, probably because the negatively charged chloride ions hamper the impregnation of the carbon support by Nafion® oligomers during the MEA processing. In addition, in the latter conditions, the cleaning/removal of the Cl-poisoning species is more difficult than in liquid electrolyte, because the limited amount of water within the active layer prevents Cl⁻ diffusion away from the Pt surface.

This study also shows that the Pt surface area measurement can be significantly biased by the measurement technique. In gas phase CO chemisorption experiments, the adsorption equilibrium must be reached before any additional CO is injected in the measurement cell: these conditions yield displacement of Cl⁻ ions by CO, and overestimation of the electrochemically active Pt surface area. In the case of CO_{ads} stripping experiments (liquid phase), the electrochemically active Pt surface area progressively increases with successive measurements due to the partial cleaning of the surface at every CO chemisorption step.

Last but not least, this study shows that very small quantities of residual Cl⁻ ions lead to a very pronounced decrease of the catalytic performance of Pt/C catalysts in PEM fuel cells. In search for efficient catalysts, chlorinated metal precursors must be avoided.

Acknowledgements

N.J. thanks the F.R.S.-FNRS (Belgium) for a post-doctoral fellowship grant, the Fonds de Recherche Fondamentale Collective (FRFC n°2.4.542.10.F), the Ministère de la Région Wallonne (project INNOPEM n°1117490), the Fonds de Bay and the Interuniversity Attraction Pole (IAP-P6/17) for their financial support. S.H. thanks the F.R.S.-FNRS (Belgium) for funding. M.C. and F.M. thank the French ANR (Suricat project) and OSEO (H2E project) for funding.

References

- [1] F. Rodríguez-Reinoso, A. Sepúlveda-Escribano, in: P. Serp, J.L. Figueiredo (Eds.), Carbon Materials for Catalysis, John Wiley & Sons, Hoboken (NJ), 2009, pp. 131–155.
- [2] X. Hao, S. Barnes, J.R. Regalbuto, *J. Catal.* 279 (2011) 48–65.
- [3] J.H. Bitter, K.P. de Jong, in: P. Serp, J.L. Figueiredo (Eds.), Carbon Materials for Catalysis, John Wiley & Sons, Hoboken, NJ, 2009, pp. 157–173.
- [4] J.R. Regalbuto, in: K.P. de Jong (Ed.), Synthesis of Solid Catalysts, Wiley-VCH, Weinheim, Germany, 2009, pp. 33–57.
- [5] E. Billy, F. Maillard, A. Morin, L. Guetaz, F. Emieux, C. Thurier, P. Doppelt, S. Donet, S. Mailley, *J. Power Sources* 195 (2010) 2737–2746.
- [6] A. Caillard, P. Brault, J. Mathias, C. Charles, R.W. Boswell, T. Sauvage, *Surf. Coat. Technol.* 200 (2005) 391–394.
- [7] A. Caillard, C. Coutanceau, P. Brault, J. Mathias, J.M. Léger, *J. Power Sources* 162 (2006) 66–73.
- [8] P. Brault, A. Caillard, A.L. Thomann, J. Mathias, C. Charles, R.W. Boswell, S. Escrivano, J. Durand, T. Sauvage, *J. Phys. D* 37 (2004) 3419–3423.
- [9] S.S. Kocha, in: W. Vielstich, A. Lamm, H. Gasteiger (Eds.), Handbook of Fuel Cells – Fundamentals, Technology and Applications, vol. 3, Wiley, Chichester, UK, 2003, pp. 538–565.

[10] H.A. Gasteiger, W. Gu, R. Makharia, M.F. Mathias, B. Sompalli, in: W. Vielstich, A. Lamm, H.A. Gasteiger (Eds.), *Handbook of Fuel Cells – Fundamentals, Technology and Applications*, vol. 3, Wiley, Chichester, UK, 2003, pp. 593–610.

[11] M. Chatenet, L. Dubau, N. Job, F. Maillard, *Catal. Today* 156 (2010) 76–86.

[12] J. Marie, S. Berthon-Fabry, P. Achard, M. Chatenet, A. Pradourat, E. Chainet, *J. Non-Cryst. Solids* 350 (2004) 88–96.

[13] J. Marie, R. Chenitz, M. Chatenet, S. Berthon-Fabry, N. Cornet, P. Achard, *J. Power Sources* 190 (2009) 423–434.

[14] M. Uchida, Y. Fukuoka, Y. Sugawara, N. Eda, A. Ohta, *J. Electrochem. Soc.* 143 (1996) 2245–2252.

[15] M. Uchida, Y. Fukuoka, Y. Sugawara, H. Ohara, A. Ohta, *J. Electrochem. Soc.* 145 (1998) 3708–3713.

[16] H.A. Gasteiger, S.S. Kocha, B. Sompalli, F.T. Wagner, *Appl. Catal., B* 56 (2005) 9–35.

[17] M. Ouattara-Brigaudet, S. Berthon-Fabry, C. Beauger, M. Chatenet, N. Job, M. Sennour, P. Achard, *Int. J. Hydrogen Energy* 37 (2012) 9742–9757.

[18] N. Job, J. Marie, S. Lambert, S. Berthon-Fabry, P. Achard, *Energy Convers. Manage.* 49 (2008) 2461–2470.

[19] C. Alegre, L. Calvillo, R. Moliner, J.A. González-Expósito, O. Guillén-Villafuerte, M.V. Martínez Huerta, E. Pastor, M.J. Lázaro, *J. Power Sources* 196 (2011) 4226–4235.

[20] N. Job, R. Pirard, J. Marien, J.-P. Pirard, *Carbon* 42 (2004) 619–628.

[21] N. Job, A. Théry, R. Pirard, J. Marien, L. Kocon, J.-N. Rouzaud, F. Béguin, J.-P. Pirard, *Carbon* 43 (2005) 2481–2494.

[22] N. Job, B. Heinrichs, S. Lambert, J.-P. Pirard, J.-F. Colomer, B. Vertruyen, J. Marien, *AIChE J.* 52 (2006) 2663–2676.

[23] N. Job, S. Lambert, M. Chatenet, C.J. Gommes, F. Maillard, S. Berthon-Fabry, J.R. Regalbuto, J.-P. Pirard, *Catal. Today* 150 (2010) 119–127.

[24] S. Lambert, N. Job, L. D'Souza, M.F.R. Pereira, R. Pirard, B. Heinrichs, J.L. Figueiredo, J.-P. Pirard, J.R. Regalbuto, *J. Catal.* 261 (2009) 23–33.

[25] J.R. Regalbuto, in: J.R. Regalbuto (Ed.), *Catalyst Preparation: Science and Engineering*, CRC Press, Taylor & Francis Group, Boca Raton, 2007, pp. 297–318.

[26] M.S. Contreras, C. Páez, L. Zubizarreta, A. Léonard, C. Olivera, S. Blacher, J.-P. Pirard, N. Job, *Carbon* 48 (2010) 3157–3168.

[27] S.A. Al-Muhtaseb, J.A. Ritter, *Adv. Mater.* 23 (2011) 2887–2903.

[28] R. Sellin, C. Grolleau, S. Arrii-Clacens, S. Pronier, J.M. Clacens, C. Coutanceau, J.M. Léger, *J. Phys. Chem. C* 113 (2009) 21735–21744.

[29] N. Job, M.F.R. Pereira, S. Lambert, A. Cabiac, G. Delahay, J.-F. Colomer, J. Marien, J.L. Figueiredo, J.-P. Pirard, *J. Catal.* 240 (2006) 160–171.

[30] G. Bergeret, P. Gallezot, in: G. Ertl, H. Knözinger, J. Weitkamp (Eds.), *Handbook of Heterogeneous Catalysis*, Wiley-VCH, Weinheim, 1997, pp. 439–464.

[31] J.R. Anderson, *Structure of Metallic Catalysts*, Academic Press, London, 1975.

[32] S. Trasatti, *J. Electroanal. Chem.* 327 (1992) 353–376.

[33] A.J. Bard, L.R. Faulkner, *Electrochemical Methods: Fundamentals and Applications*, Wiley, New York, 1992, p. 283.

[34] F. Rodríguez-Reinoso, I. Rodríguez-Ramos, C. Moreno-Castilla, A. Guerrero-Ruiz, J.D. López-González, *J. Catal.* 99 (1986) 171–183.

[35] Y. Takasu, N. Ohashi, X.G. Zhang, Y. Murakami, H. Minagawa, S. Sato, K. Yahikozawa, *Electrochim. Acta* 41 (1996) 2595–2600.

[36] O. Antoine, Y. Bultel, R. Durand, P. Ozil, *Electrochim. Acta* 43 (1998) 3681–3691.

[37] K. Kinoshita, *J. Electrochem. Soc.* 137 (1990) 845–848.

[38] F. Maillard, S. Pronkin, E.R. Savinova, in: W. Vielstich, H.A. Gasteiger, H. Yokokawa (Eds.), *Handbook of Fuel Cells – Electrocatalysis, Materials, Diagnostics and Durability*, vol. 5, John Wiley & Sons, New York, 2009, pp. 91–111.

[39] F. Maillard, M. Eikerling, O.V. Cherstiouk, S. Schreier, E. Savinova, U. Stimming, *Faraday Discuss.* 125 (2004) 357–377.

[40] F. Maillard, S. Schreier, M. Hanzlik, E.R. Savinova, S. Weinkauf, U. Stimming, *Phys. Chem. Chem. Phys.* 7 (2005) 385–393.

[41] F. Maillard, E.R. Savinova, U. Stimming, *J. Electroanal. Chem.* 599 (2007) 221–232.

[42] B. Andreus, F. Maillard, J. Kocyo, E.R. Savinova, M. Eikerling, *J. Phys. Chem. B* 110 (2006) 21028–21040.

[43] M.J. Martínez-Rodríguez, E.B. Fox, W.D. Rhodes, C.S. McWorther, S. Greenway, H.R. Colón-Mercado, *J. Electrochem. Soc.* 158 (2011) B698–B702.

[44] J.Z. Zhang, H.R. Colón-Mercado, J.G. Goodwin Jr., *J. Power Sources* 196 (2011) 8391–8397.

[45] M.W. Breiter, *Electrochim. Acta* 8 (1962) 925–935.

[46] V.S. Bagotsky, Y.B. Vassilyev, J. Weber, J.N. Pirtskhalava, *J. Electroanal. Chem.* 27 (1970) 31–46.

[47] T.J. Schmidt, U.A. Paulus, H.A. Gasteiger, R.J. Behm, *J. Electroanal. Chem.* 508 (2001) 41–47.

[48] T.M. Arruda, B. Shyam, J.M. Ziegelbauer, S. Mukerjee, D.E. Ramaker, *J. Phys. Chem. C* 112 (2008) 18087–18097.

[49] N. Markovic, P.N. Ross, *J. Electroanal. Chem.* 330 (1992) 499–520.

[50] A.A. Holscher, W.M.H. Sachtle, *Discuss. Faraday Soc.* 41 (1966) 29–42.

[51] R. Durand, R. Faure, F. Gloaguen, D. Aberdam, in: R.R. Adzic, F.C. Anson, K. Kinoshita (Eds.), *Proceedings of the Symposium on Oxygen Electrochemistry*, vol. 95–26, The Electrochemical Society, Pennington, NJ, 1996, pp. 27–37.

[52] N.M. Markovic, T.J. Schmidt, V. Stamenovic, P.N. Ross, *Fuel Cells* 1 (2001) 105–116.

[53] L. Dubau, F. Maillard, M. Chatenet, J. André, E. Rossinot, *Electrochim. Acta* 56 (2010) 776–783.